Supplemental Figure 1

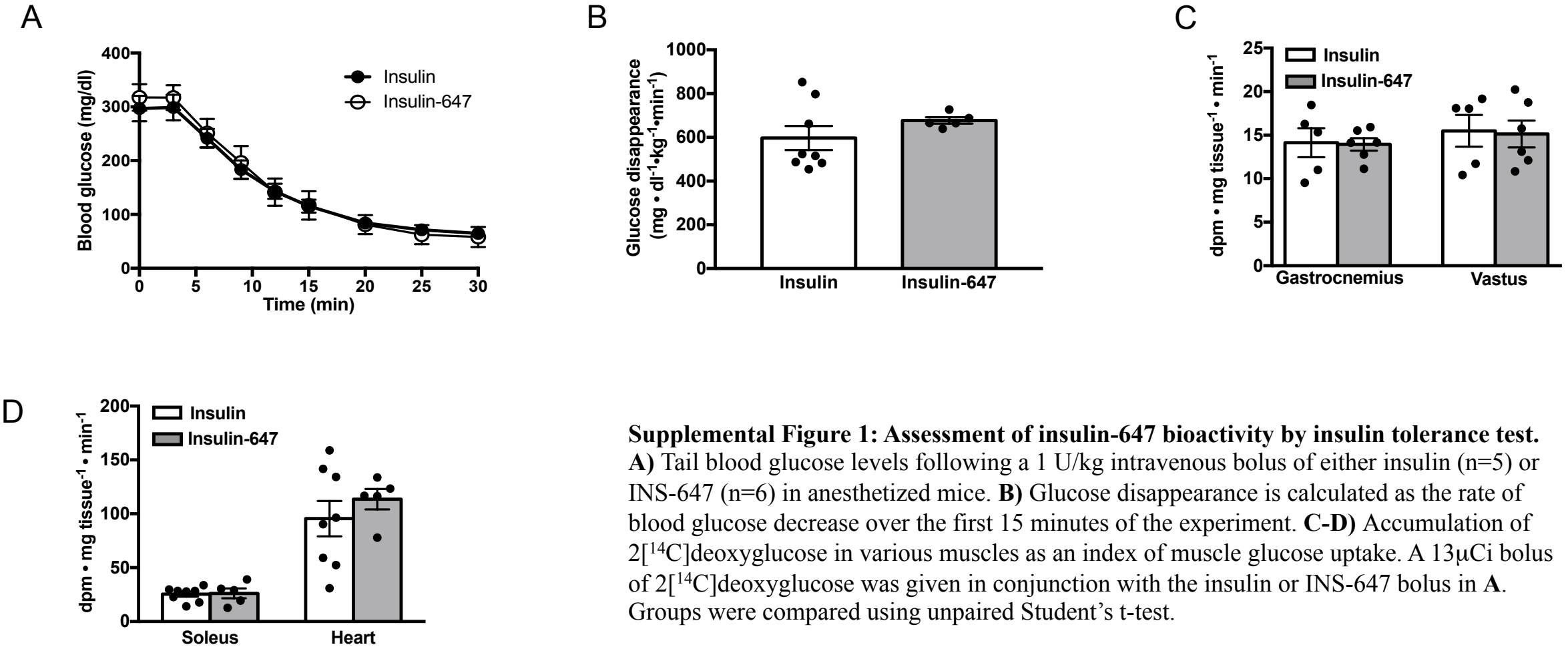

Supplemental Figure 1: Assessment of insulin-647 bioactivity by insulin tolerance test. **A)** Tail blood glucose levels following a 1 U/kg intravenous bolus of either insulin (n=5) or INS-647 (n=6) in anesthetized mice. **B)** Glucose disappearance is calculated as the rate of blood glucose decrease over the first 15 minutes of the experiment. **C-D)** Accumulation of 2[^{14}C]deoxyglucose in various muscles as an index of muscle glucose uptake. A 13μCi bolus of 2[^{14}C]deoxyglucose was given in conjunction with the insulin or INS-647 bolus in **A**. Groups were compared using unpaired Student's t-test.

Supplemental Figure 2

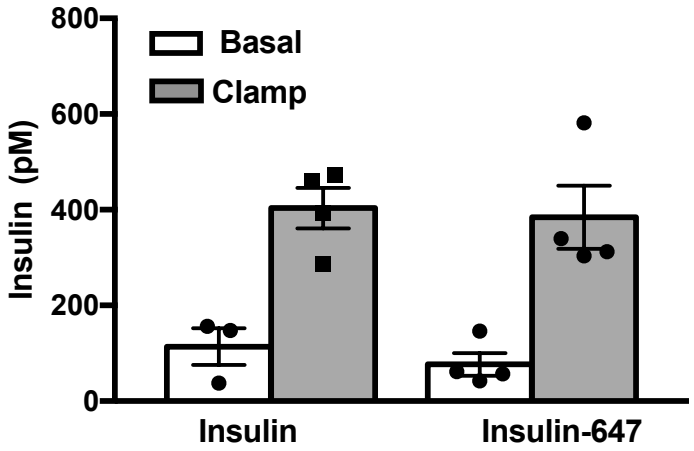

Supplemental Figure 2: Plasma insulin levels during hyperinsulinemic-euglycemic clamps. Basal and clamp levels of plasma insulin during hyperinsulinemic-euglycemic clamps with either insulin (n=4) or INS-647 (n=4). Groups were compared using unpaired Student's t-test.

Supplemental Figure 3

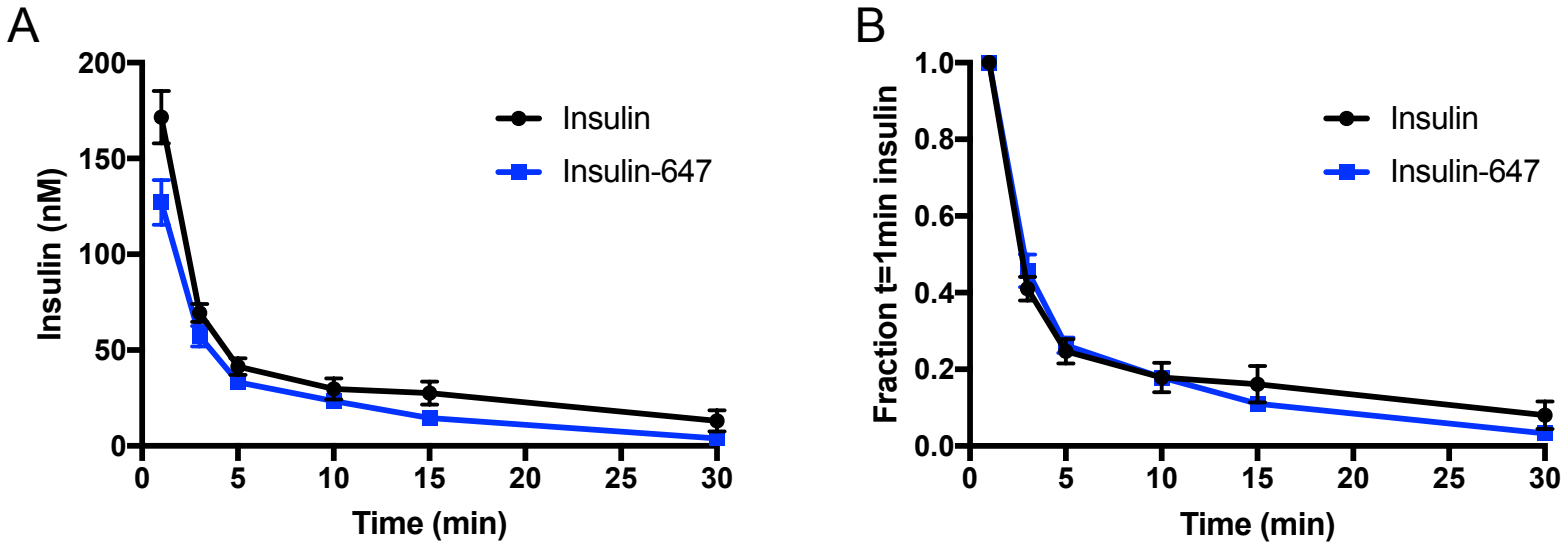

Supplemental Figure 3: Arterial dynamics of insulin-647 and unlabeled insulin. **A)** Arterial plasma levels of insulin (n=6) and insulin-647 (n=6) following a 4U/kg intravenous bolus. **B)** Data in **A** normalized to the insulin level at t=1 min.

Supplemental Figure 4

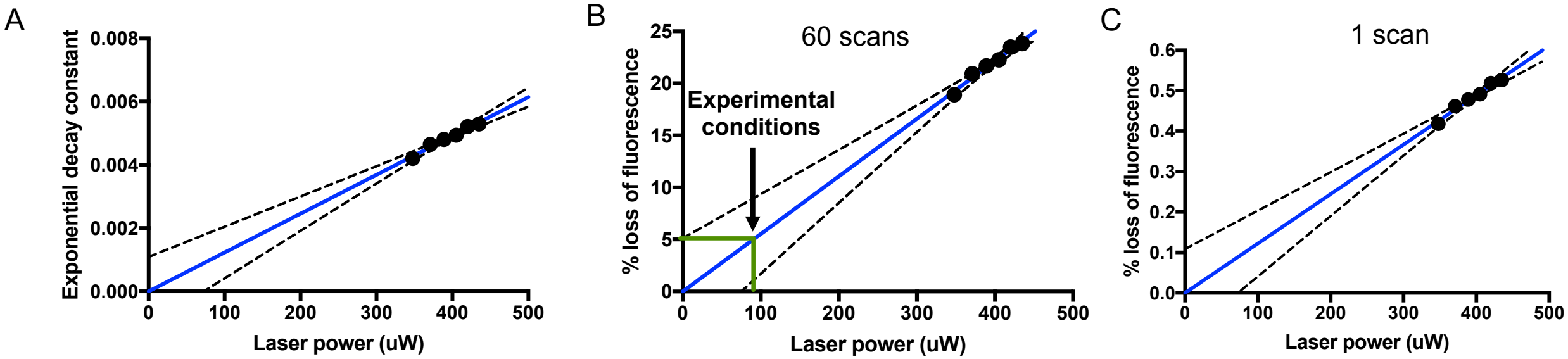

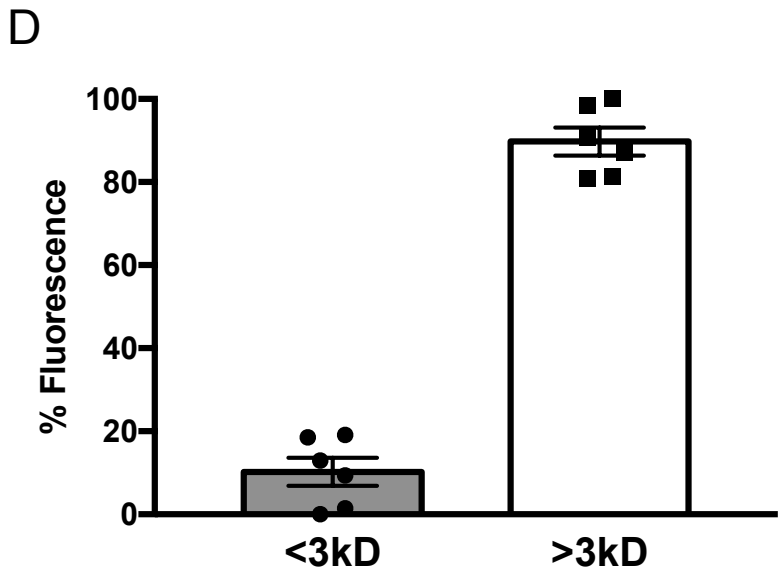

Supplemental Figure 4: Photostability and *in vivo* stability of insulin-647. A) The rate of decay of INS-647 fluorescence as a function of incident laser power. The blue line shows the linear regression of these two variables and the dotted lines show the 95% confidence intervals of the regression. **B)** % loss of fluorescence after 60 scans, the same number of scans as during an insulin imaging experiment. The green lines indicate the maximum usable laser power at which the acceptable photobleaching rate (5%) is achieved. **C)** % loss of fluorescence per scan. **D)** % of total plasma INS-647 fluorescence that is in a low molecular weight fraction (<3kD) vs. a high molecular weight fraction (>3kD) 30 minutes after an intravenous bolus of INS-647 (n=6 mice). Fluorescence in the <3kD fraction is indicative of Alexa Flour 647 that is separated from INS-647 during an imaging experiment. Fluorescence in the >3kD fraction is intact INS-647. Plasma from n=6 mice was used for determination *in vivo* stability of INS-647.

Supplemental Figure 5

A

%CD45+ R6G+ cells

Replicate	5 min	30 min
a	95.3	89.9
b	94.6	89.2
c	92.3	85.6

B

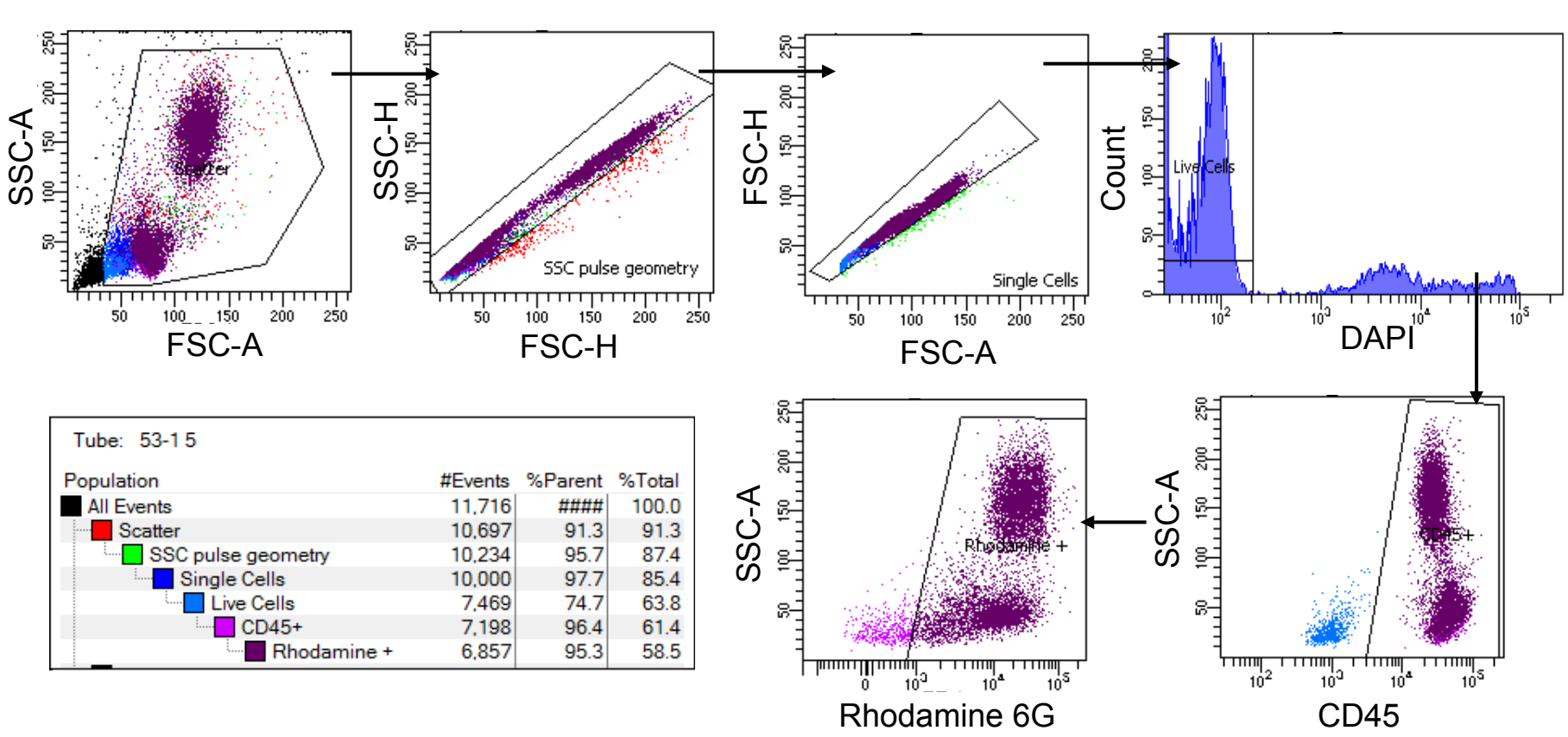

Supplemental Figure 5: Labeling efficiency of leukocytes *in vivo* with rhodamine 6G. A) Table shows the % of live leukocytes that are stained with rhodamine 6G at two time points following rhodamine 6G injection (n=3 mice). **B)** Gating strategy for flow cytometry. In the direction of the arrows, debris were removed by size, doublets were deleted (2x), and dead cells were removed (DAPI). The remaining cells were gated for presence of CD45 to include leukocytes and finally the % of these leukocytes containing rhodamine 6G was measured. R6G, rhodamine 6G.

Supplemental Figure 6

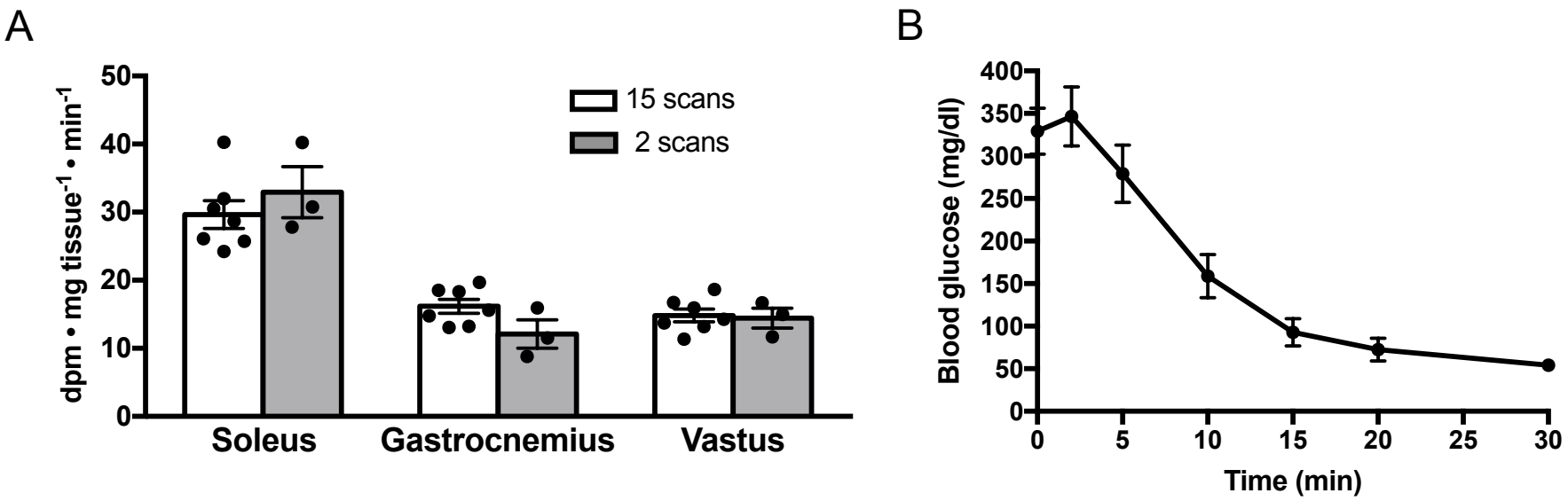

Supplemental Figure 6: Effect of varying light exposure on insulin-stimulated muscle glucose uptake. **A)** Accumulation of 2[^{14}C]deoxyglucose in various tissues during INS-647 imaging with either 2 (n=3) exposures or 15 exposures (n=7). **B)** Whole blood glucose excursions following a 4U/kg insulin bolus in anesthetized mice (n=4).

Supplemental Figure 7

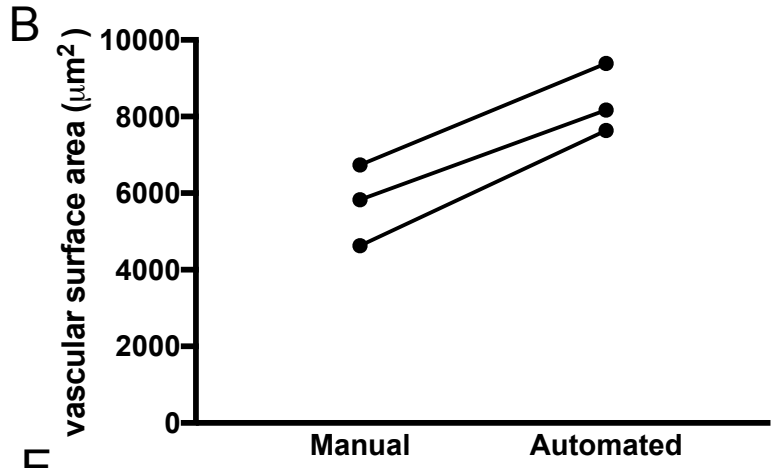

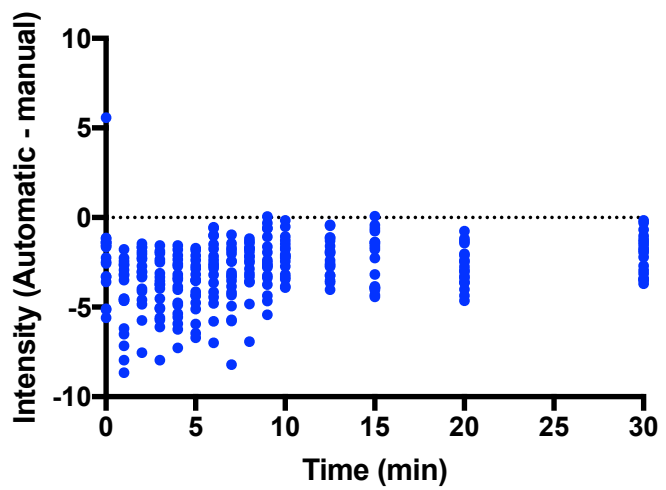

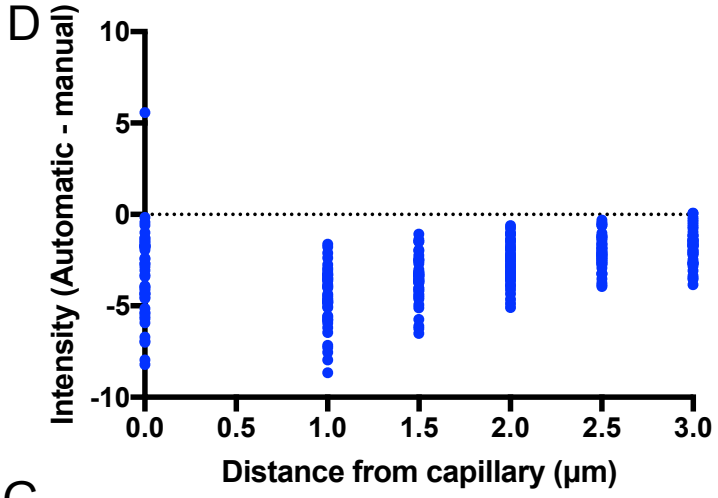

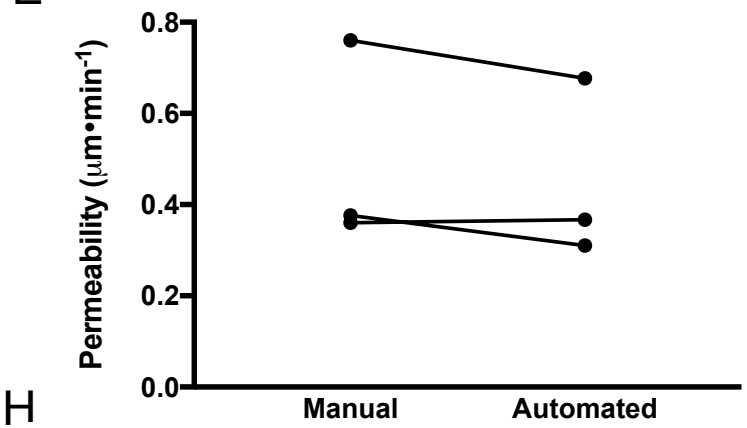

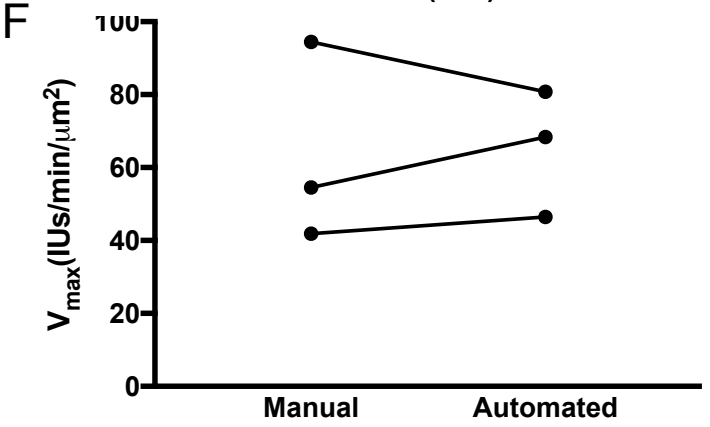

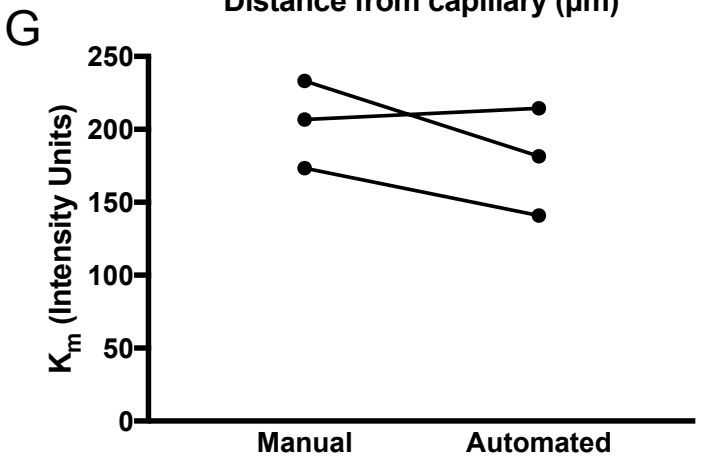

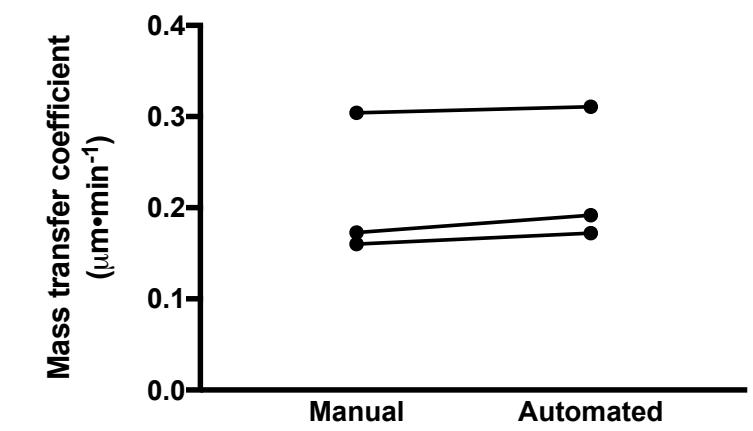

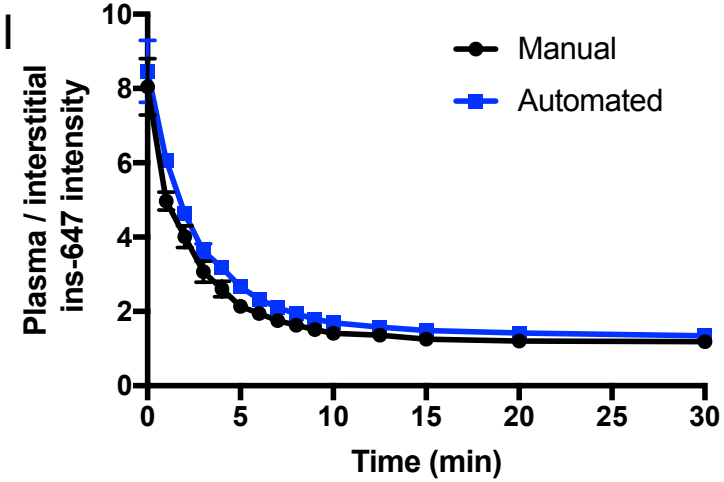

Supplemental Figure 7: Performance of an automated vascular segmentation algorithm. The segmentation performance of an automated algorithm was compared against manual segmentation for all images from n=3 experiments. **A)** Percent of manually outlined pixels that were also outlined by the algorithm (True positive) and percent of pixels outlined by the algorithm that were not outlined by the manual segmentation (False positive). **B)** Total vascular surface area segmented by manual and automated segmentation. **C,D)** Difference in INS-647 intensity as a function of **C)** time or **D)** distance from the capillary when using automated versus manual segmentation. **E-H)** Best fit model parameter estimates using manual or automated segmentation. **I)** Ratio of plasma to interstitial INS-647 intensity as a function of time following ins-647 injection using manual and automated segmentation.

Supplemental Figure 8

Parameter	Estimate
K_m	222.1 ± 25.8 IU
V_{max}	77.2 ± 13.5 IU/min/μm^2
Interstitial diffusion coefficient	1.64 ± 0.16 μm^2/min
Removal constant	0.056 ±0.003 1/min

Supplemental Figure 8: Michaelis-Menten model parameter estimates. Best-fit Michaelis-Menten model parameter estimates for a cohort of n=6 mice. Data are mean ± standard error. K_m - substrate concentration at which the reaction rate is half of V_{max}. V_{max} – maximum reaction rate.

Supplemental Figure 9

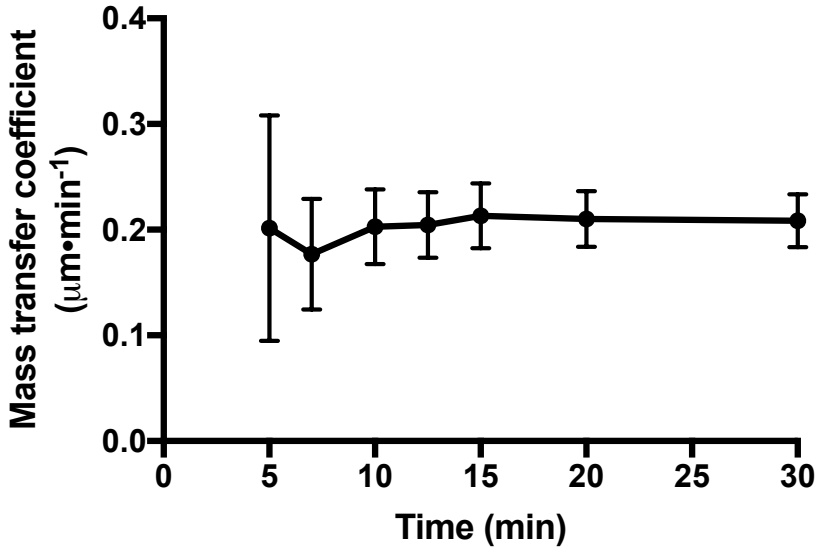

Supplemental Figure 9: Temporal stability of the mass transfer coefficient. Best-fit mass transfer coefficient estimates from temporal subsets of INS-647 imaging experiments (n=6 mice). The x-axis represents the final time point included in subsequent mathematical modeling.

Supplemental Figure 10

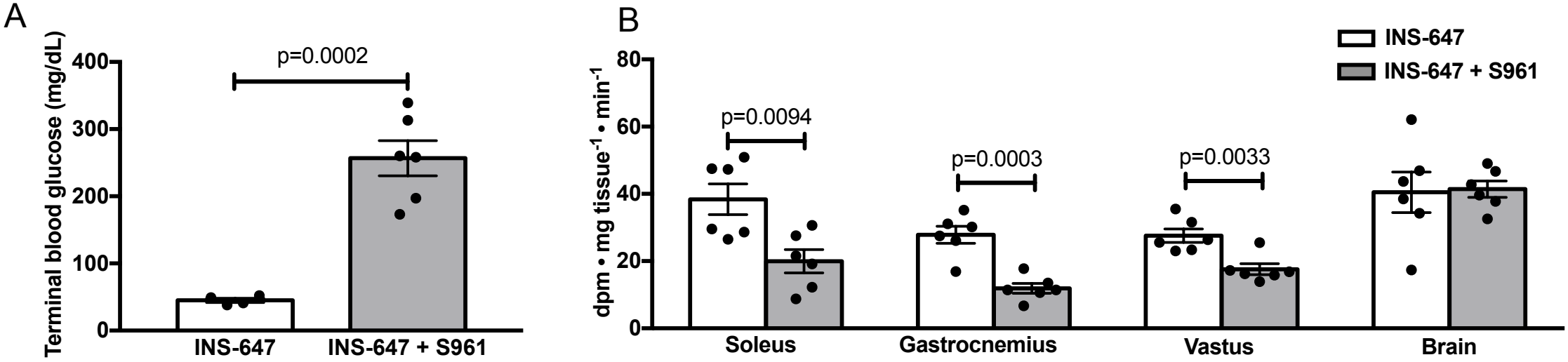

Supplemental Figure 10: Effects of S961 on insulin-stimulated glucose kinetics. A) Tail vein blood glucose levels following an INS-647 imaging experiment in mice treated either with a 4U/kg INS-647 bolus alone (INS-647; n=4) or with an insulin receptor antagonist followed by the 4U/kg INS-647 bolus (INS-647 + S961; n=6). **B)** Accumulation of 2[^{14}C]deoxyglucose in various tissues during INS-647 imaging in mice treated with (INS-647 + S961; n=6) or without (INS-647; n=6) the insulin receptor antagonist. Groups were compared using unpaired Student's t-test.

Supplemental Figure 11

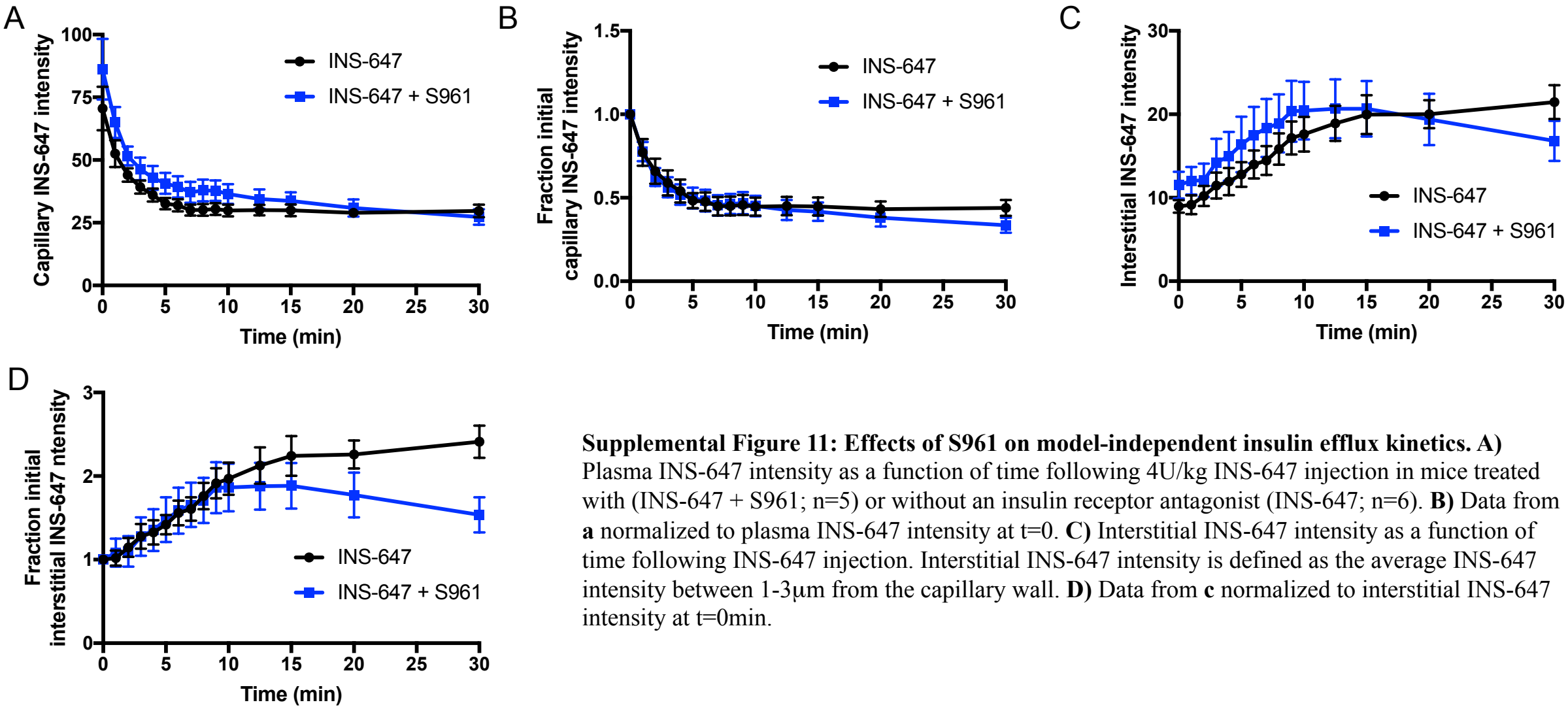

Supplemental Figure 11: Effects of S961 on model-independent insulin efflux kinetics. A) Plasma INS-647 intensity as a function of time following 4U/kg INS-647 injection in mice treated with (INS-647 + S961; n=5) or without an insulin receptor antagonist (INS-647; n=6). **B)** Data from **a** normalized to plasma INS-647 intensity at t=0. **C)** Interstitial INS-647 intensity as a function of time following INS-647 injection. Interstitial INS-647 intensity is defined as the average INS-647 intensity between 1-3μm from the capillary wall. **D)** Data from **c** normalized to interstitial INS-647 intensity at t=0min.

Supplemental Figure 12

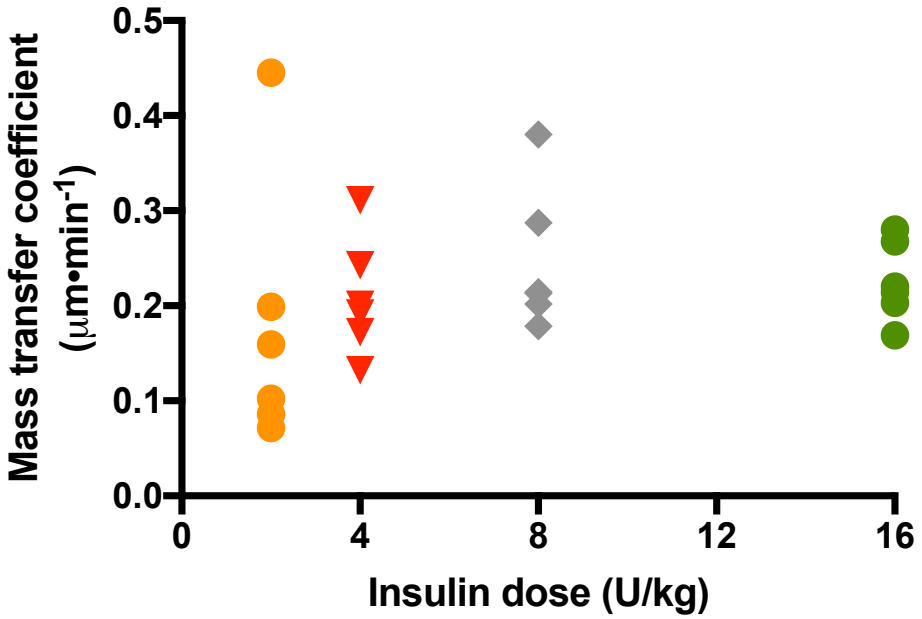

Supplemental Figure 12: Effects of insulin dose on the mass transfer coefficient estimate. Best-fit fluid-phase transport model estimates of the mass transfer coefficient in mice treated with 2U/kg INS-647 (n=6), 4U/kg INS-647 (n=6), 4U/kg INS-647 and 4U/kg unlabeled insulin (n=6), or 4U/kg INS-647 and 12U/kg unlabeled insulin (n=6). For mice treated with 0.5U/kg or 1U/kg INS-647, the image signal-to-noise ratio was too low to allow for mathematical modeling.

Supplemental Figure 13

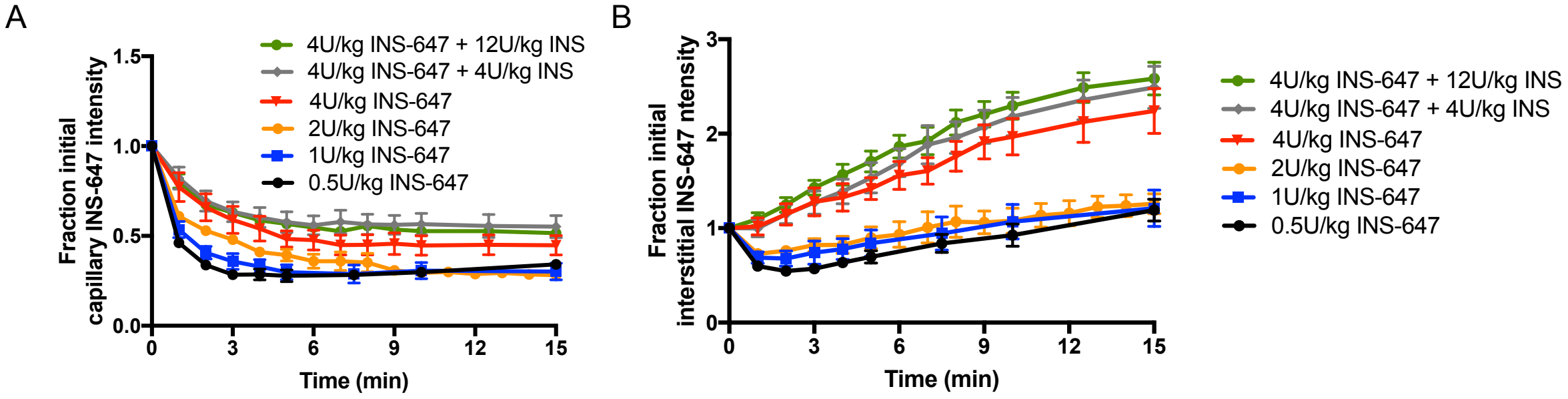

Supplemental Figure 13: Effects of insulin dose on model-independent insulin efflux kinetics. A) Plasma INS-647 intensity as a function of time following INS-647 injection in mice treated with either 0.5U/kg INS-647 (n=7), 1U/kg INS-647 (n=7), 2U/kg INS-647 (n=6), 4U/kg INS-647 (n=6), 4U/kg INS-647 and 4U/kg unlabeled insulin (n=6), or 4U/kg INS-647 and 12U/kg unlabeled insulin (n=6). Data are normalized to capillary INS-647 at t=0. **B)** Normalized interstitial INS-647 intensity as a function of time following INS-647 injection. Interstitial INS-647 intensity is defined as the average INS-647 intensity between 1-3μm from the capillary wall. Data are normalized to interstitial INS-647 intensity at t=0.

Supplemental Figure 14

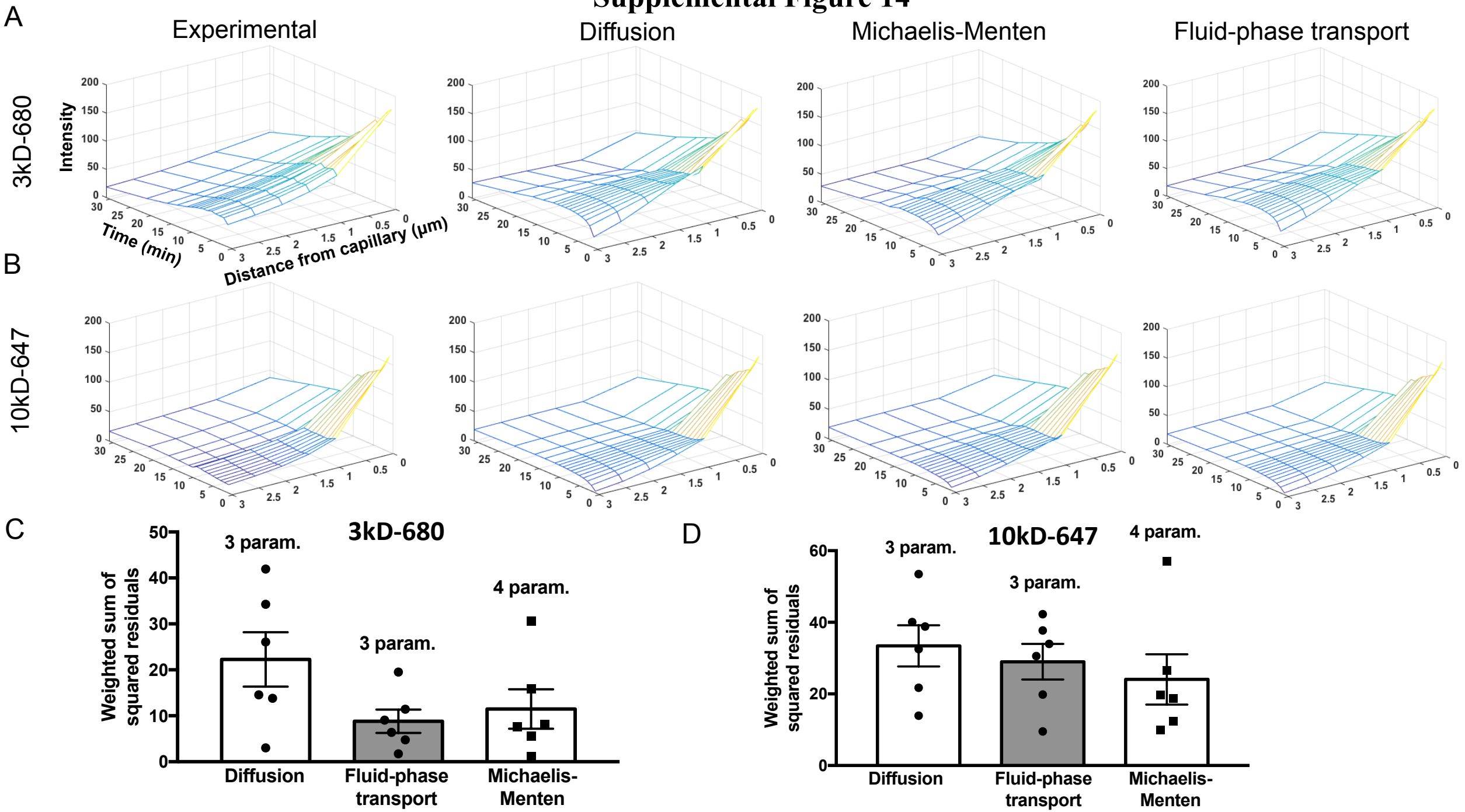

Supplemental Figure 14: Model fit analysis of inert tracer data. Plots show experimental data and "Diffusion," "Michaelis-Menten," or "Fluid-phase transport" model simulations for **A)** 3kD dextran-Alexa Fluor 680 and **B)** 10kD dextran-Alexa Fluor 647 probe. **C,D)** Weighted sum of squared residuals for each of the different model simulations as compared to the experimental data for **C)** 3kD dextran-Alexa Fluor 680 (n=6) and **D)** 10kD dextran-Alexa Fluor 647 (n=6). The number of variable parameters are indicated above the bar for each model. Param – parameters.